

1 **Hiss or Equatorial Noise? Ambiguities in Analyzing**
2 **Suprathermal Ion Plasma Wave Resonance**

Lois K. Sarno-Smith¹, Michael W. Liemohn¹, Ruth M. Skoug², Ondrej

Santolik^{3,4}, Steven K. Morley², Aaron Breneman⁵, Brian A. Larsen², Geoff

Reeves², John R. Wygant⁵, George Hospodarsky⁶, Craig Kletzing⁶, Mark B.

Moldwin¹, Roxanne M. Katus¹, Shasha Zou¹

Author Manuscript

Corresponding author: Lois K. Sarno-Smith, Department of Climate and Space Sciences and Engineering, University of Michigan, Ann Arbor, Michigan, USA. (loisks@umich.edu)

¹Department of Climate and Space

This is the author manuscript accepted for publication and has undergone full peer review but has not been through the copyediting, typesetting, pagination and proofreading process, which may lead to differences between this version and the Version of Record. Please cite this article

as doi:10.1002/2016JA022995 September 23, 2016, 11:12pm

D R A F T

Abstract.

Previous studies have shown that low energy ion heating occurs in the magnetosphere due to strong equatorial noise emission. Observations from the Van Allen Probes Helium Oxygen Proton Electron (HOPE) instrument recently determined there was a depletion in the 1-10 eV ion population in the post-midnight sector of Earth during quiet times at $L < 3$. The diurnal variation of equatorially mirroring 1-10 eV H^+ ions between $2 < L < 3$ is connected with similar diurnal variation in the electric field component of plasma

Sciences and Engineering, University of Michigan, Ann Arbor, Michigan, USA.

²Los Alamos National Laboratory, Los Alamos, New Mexico, USA.

³Department of Space Physics, Institute of Atmospheric Physics CAS, Prague

⁴ Faculty of Mathematics and Physics, Charles University in Prague

⁵School of Physics and Astronomy, University of Minnesota, Minneapolis, Minnesota USA.

⁶Department of Physics and Astronomy, University of Iowa, Iowa City, Iowa, USA.

11 waves ranging between 150 and 600 Hz. Measurements from the Van Allen
12 Probes Electric and Magnetic Field Instrument Suite and Integrated Science
13 (EMFISIS) data set are used to analyze waves of this frequency in near-Earth
14 space. However, when we examine the polarization of the waves in the 150
15 to 600 Hz range in the equatorial plane, the majority are right-hand polar-
16 ized plasmaspheric hiss waves. The 1-10 eV H⁺ equatorially mirroring pop-
17 ulation does not interact with right hand waves, despite a strong statistical
18 relationship suggesting the two is linked. We present evidence supporting the
19 relationship, both in our own work and the literature, but we ultimately con-
20 clude that the 1-10 eV H⁺ heating is not related to the strong enhancement
21 of 150 to 600 Hz waves.

22

Author Manuscript

1. Introduction

23 Thermal ions in the plasmasphere have been shown to be transversely heated through
24 ion cyclotron resonance with waves above the ion gyrofrequency and below the lower
25 hybrid resonant frequency. Ion cyclotron resonant heating of thermal ions was demon-
26 strated through observations and modeling of GEOS-1 and GEOS-2 data [Young *et al.*,
27 1981; Rouss *et al.*, 1982; Perraut *et al.*, 1982; Perraut, 1982]. In particular, He⁺ was shown
28 to most strongly resonate with the measured frequencies in the GEOS data. Other stud-
29 ies concluded that cyclotron resonance heats H⁺ thermal populations at geosynchronous
30 orbit similar to the He⁺ heated population [Quinn and Johnson, 1982]. These thermal
31 ions require left hand or linearly polarized waves for wave-particle interactions that lead
32 to subsequent heating. However, there is still debate as to which waves are present during
33 times of inner magnetosphere low energy ion heating: equatorial noise or plasmaspheric
34 hiss.

35
36 Equatorial noise has been shown to heat thermal ions through cyclotron resonance
37 [Olsen *et al.*, 1987; Singh and Hwang, 1987; Laakso *et al.*, 1990]. Equatorial noise is a
38 fast magnetosonic, low frequency wave with nearly linearly polarized magnetic field fluc-
39 tuations generated by unstable energetic proton ring velocity distributions [Perraut *et al.*,
40 1982; Gary *et al.*, 2010]. Equatorial noise ranges in frequency from approximately 20
41 Hz to a few hundred Hz and lies below the lower hybrid frequency [Němec *et al.*, 2015;
42 Boardman *et al.*, 2016]. Typically, equatorial noise is found between 2 and 7 Earth radii
43 and within 10 degrees of the magnetic equator [Russell *et al.*, 1970; Němec *et al.*, 2006].

44 Strong diurnal variation has been previously seen in Cluster observations of equatorial
45 noise outside of the plasmasphere, with a peak at MLT = 12 and a minimum in the post-
46 midnight sector between MLT = 0 and 6 [Hrbáčková *et al.*, 2015; Ma *et al.*, 2016]. Studies
47 of the global wave distribution revealed that equatorial magnetosonic waves inside the
48 plasmapause depended on substorm activity and had larger amplitudes and higher occur-
49 rence frequencies on the dayside [Green *et al.*, 2005; Meredith *et al.*, 2008; Ma *et al.*, 2013].

50
51 Based on Dynamics Explorer 1 and SCATHA observations, it was proposed that equa-
52 torial noise, generated by highly energetic ions in the ring current and/or radiation belt,
53 heats the thermal ion population through cyclotron resonance. Wave-particle interactions
54 elevate the thermal population to a suprathermal population via energy deposition by
55 equatorial noise ($10 \text{ eV} < E < 300 \text{ eV}$) [Curtis, 1985]. The energy transference could also
56 occur with $1-10 \text{ eV He}^+$ and O^+ , albeit on slower time scales. Modeling work also suggests
57 that inward propagating magnetosonic waves produced by proton ring instabilities could
58 cause thermal plasma heating near-Earth [Horne *et al.*, 2000].

59
60 However, plasmaspheric hiss occupies a similar region of space as the equatorial noise
61 and typically ranges from 20 Hz to approximately 1000 Hz [Thorne *et al.*, 1973; Meredith
62 *et al.*, 2007; Li *et al.*, 2015]. Plasmaspheric hiss is a broadband incoherent electromagnetic
63 emission that is largely confined to Earth's plasmasphere [Meredith *et al.*, 2009]. Plasma-
64 spheric hiss can be generated from magnetospherically reflecting whistler waves or from
65 inward propagating chorus emissions that lose coherency when they cross the plasmapause
66 [Draganov *et al.*, 1992; Bortnik *et al.*, 2008]. Hiss amplification at the equator due to wave

67 turbulence from the electron gyroresonance instability leads to enhanced plasmaspheric
68 hiss in the magnetic equatorial plane [*Thorne and Barfield, 1976; Church and Thorne,*
69 *1983; Solomon et al., 1988; Santolik et al., 2001*]. Unlike equatorial noise, plasmaspheric
70 hiss is right hand polarized and primarily interacts with electrons [*Tsurutani et al., 1975;*
71 *Li et al., 2007; Summers et al., 2007*]. Without looking at polarization or spectral lines, it
72 is difficult to distinguish between plasmaspheric hiss and equatorial noise [*Gurnett, 1976;*
73 *Santolik et al., 2002*].

74
75 Plasma waves are a likely cause for the observed minimum in the high energy tail (1-10
76 eV) of the inner plasmasphere (L-Shell < 3) in the post-midnight sector [*Lennartsson*
77 *and Reasoner, 1978; Sarno-Smith et al., 2015*]. A previous study revealed that in the
78 post-midnight sector specifically, the H⁺ pitch angle (PA) = 90° population between 2 <
79 L < 3 was depleted but plasma was still flowing upward from the ionosphere [*Sarno-Smith*
80 *et al., 2015a*]. Upward flowing plasma in the post-midnight sector suggests that the ap-
81 parent loss of plasma in the post-midnight sector is not driven by the cooling of plasma
82 in the topside ionosphere. Instead, plasma wave influence may be heating/scattering the
83 particles in such a way to lead to strong diurnal variation in the 1-10 eV population.

84
85 Three instruments onboard the NASA Van Allen Probes mission enable further explo-
86 ration of the connection between 1-10 eV ions of the inner plasmasphere and plasma wave
87 activity. The Van Allen Probes, launched in late 2012, are a pair of satellites that are
88 in highly elliptical, low inclination orbits [*Mauk et al., 2014*]. The Electric and Magnetic
89 Field Instrument Suite and Integrated Science (EMFISIS) instrument measures plasma

90 waves between approximately 2 Hz and 12 kHz using three search coil magnetometers and
91 the three Electric Field and Waves (EFW) instrument's electric field antennas [*Wygant*
92 *et al.*, 2013; *Kletzing et al.*, 2014]. EMFISIS also measures the DC magnetic field with
93 onboard magnetometers. The plasma wave range we examine is between 150 Hz and 600
94 Hz, well within the resolution capabilities of EFW and EMFISIS. The Helium Oxygen
95 Proton Electron (HOPE) instrument measures the ion and electron populations of the
96 equatorial inner magnetosphere between 1 eV and 50 keV [*Funsten et al.*, 2014]. HOPE
97 also uses the EMFISIS magnetometer measurements to map the observed fluxes into pitch
98 angle space and assign nominal pitch angle bins.

99
100 We examine the connection between 150 Hz - 600 Hz waves with the 1-10 eV ion pop-
101 ulation of the $L < 3$ inner plasmasphere. As previous studies have found, we find the
102 diurnal variation in the 150 Hz - 600 Hz waves is linked with the 1-10 eV ion equatorially
103 mirroring population growth and loss [*Olsen et al.*, 1987; *Singh and Hwang*, 1987]. Po-
104 larization analysis reveals that the near-Earth emissions near the equator are primarily
105 plasmaspheric hiss and do not cyclotron resonate with the low energy ions and are not re-
106 sponsible for the ion heating. We corroborate our results with observations from EMFISIS
107 and HOPE, opening up several questions in magnetospheric physics of our understanding
108 of thermal plasma and wave interaction.

109 2. Particle and Wave Statistics

110 Following the 1-10 eV ion depletion in the post-midnight sector discovery in *Sarno-Smith*
111 *et al.* [2015], we examine the fluxes measured at different pitch angles from February 2013

112 to April 2015. The polar angle resolution on the HOPE instrument is 18 degrees full width.
113 Pitch angle bins are 18 degrees wide, except for 9 degree bins centered at 4.5 and 175.5
114 degrees. In every spin period of approximately 11 seconds, HOPE differential number
115 flux values were calculated and assigned a pitch angle designation based on the magnetic
116 field direction as measured by EMFISIS. Initial analysis of the pitch angle distributions
117 were conducted by *Sarno-Smith et al.* [2016b], and here the analysis is taken further to
118 examine the evolution of the full velocity-space distribution in both energy and pitch angle.

119
120 Figure 1 displays the median 1-10 eV H⁺ differential number fluxes at L = 2.5 for times
121 when Kp < 3 between February 2013 and April 2015 measured by HOPE sorted by pitch
122 angle, MLT, and energy. The fluxes are corrected for spacecraft charging, and the process
123 is detailed in *Sarno-Smith et al.* [2016b]. We note that the Van Allen Probes tend to
124 charge slightly positive. The L = 2.5 bin spans from 2.375 to 2.625 (0.25 L-Shell). The
125 fluxes are not always centered near-PA = 90° due to seasonal effects, such as increased
126 upwelling ion fluxes from the summer hemisphere compared to the winter hemisphere. At
127 MLT = 2, the near PA = 90° population is at a minimum for all energies shown. The flux
128 measurements at near PA = 0° and near PA = 180° are lower compared with other MLTs
129 for these pitch angle bins but are larger than the near PA = 90° measurements. The
130 equatorially mirroring population begins to refill for the 1 eV energy channels at MLT =
131 4, but the near PA = 90° population minimum is prevalent at the higher energies (energy
132 > 2 eV). MLT = 6 demarcates the transition from a dominant refilling population at 0°
133 and 180° to a more equatorially mirroring focused population. Above 6 eV, however, the
134 near PA = 90° population is still at a relative minimum compared to the 0° and 180°

135 degree pitch angle flux measurements or the distribution is isotropic.

136

137 A balance is struck between MLT = 8 to MLT = 18 where the near PA = 90° population
138 is still at a relative minimum above 8 eV, but the near PA = 90° population remains in a
139 steady state throughout the day. MLT = 22 fluxes reveal that the equatorially mirroring
140 population has begun to recede. While the near PA = 90° population still dominates be-
141 low 3 eV, the pitch angle distributions are either refilling (0°/180° dominated) or isotropic
142 beyond 3 eV. MLT = 0 exhibits similar behavior, with the last of the near PA = 90° pop-
143 ulation at 1.5 eV narrowing.

144

145 In Figure 1, there are two indications that the loss of the equatorially mirroring popula-
146 tion may not simply be a balance of ionospheric outflow and scattering. The first indicator
147 is if the change in 1.5-10 eV plasma in the inner magnetosphere was from ionospheric di-
148 urnal variation and consequent transport to the plasmasphere, it would be expected that
149 the high energy ions should appear first at L = 2.5 and scatter first since they move
150 the fastest. Instead, we see that the lowest energies for PA = 90° rise the fastest and the
151 higher energies above 8 eV either never have a near PA = 90° population maximum or take
152 longer than the lower energies. For example, the 2 eV equatorially mirroring population is
153 at a maximum by MLT = 6, but the 8 eV population is not at a maximum until MLT = 8.

154

155 The other indication is the depletion in the near PA = 90° population compared to
156 the near PA = 0°/180° measurements. While the equatorially mirroring populations have
157 > 2.5 orders of magnitude of variation, the field aligned fluxes show about 2 orders of

158 magnitude diurnal variation. We use the 18° and 162° bins to describe the field aligned
159 PA bins because the 175.5° and 4.5° bins are smaller and less accurate. Figure 2 shows
160 the $L = 2.5$ spacecraft potential corrected fluxes of 1.55, 1.83, 2.18, 2.53, 2.95, 3.38, 3.94,
161 4.64, and 5.35 eV normalized by the highest values at each energy at pitch angles of 18° ,
162 54° , 90° , 144° , and 162° . For the more field aligned pitch angles, the normalized fluxes
163 show that the high energy H^+ ions rise first at dawn compared to the slower particles. At
164 $PA = 90^\circ$, the opposite occurs, with the lowest energy fluxes increasing first.

165
166 The $PA = 90^\circ$ fluxes also show an energy dependent decrease. Starting at $MLT = 18$,
167 the $PA = 90^\circ$ fluxes start decreasing. The highest energy ions are depleted first, with over
168 an order of magnitude drop occurring before midnight. The low energy ions (1-3 eV) have
169 a delayed depletion until the post-midnight sector. The steady growth of the $PA = 90^\circ$
170 population across the morning to a saturation point at $MLT = 10$ suggests perpendicular
171 heating of the H^+ ions throughout the dayside. The flatness of the curves across the dayside
172 at all pitch angles in Figure 2 indicates that the fluxes are in equilibrium, with the wave
173 heating balanced by the scattering and loss.

174
175 From Figures 1 and 2, we can conclude that wave activity, not ionospheric breathing,
176 is responsible for the 1-10 eV ion depletion because of the behavior of the $PA = 90^\circ$
177 population. Following the theory of equatorial noise heating thermal plasma from *Olsen*
178 *et al.* [1987], we explore the possibility of a wave-particle interaction by examining the
179 EMFISIS survey mode data over the course of 26 months. The survey mode on EMFISIS
180 includes a set of spectral matrices every 6 seconds [*Kletzing et al.*, 2014]. The EMFISIS

181 instrument uses a fast Fourier transform on board to analyze the electric field samples
182 from EFW and the results are telemetered to the ground. The EMFISIS survey mode
183 data are averaged onboard into 65 logarithmically spaced bins between 2 Hz and 10 kHz
184 and binned by 0.5 MLT and 0.25 L-Shell for times when $K_p < 3$.

185
186 To identify peak wave activity, Figure 3 shows the relative intensity of EMFISIS Wave-
187 Form Receiver (WFR) frequencies as a function of MLT at $L = 2.5$. Figure 3A shows the
188 median power spectral densities from February 2013 to April 2015. Figure 3B uses the
189 same binning strategy and displays the normalized power spectral densities. The power
190 spectral densities in each frequency bin are normalized by the highest power spectral
191 density in that frequency bin. The silver line is the 6th harmonic of the H^+ cyclotron
192 frequency. We use the 6th harmonic of the H^+ cyclotron frequency because it is approx-
193 imately where we see enhanced power spectral densities. We show the geometric mean
194 lower hybrid frequency instead of the lower hybrid frequency because it is difficult to get
195 a true estimate on plasma density at $L < 3$, where EMFISIS electron number density
196 estimates from the upper hybrid frequency saturate [Kurth *et al.*, 2015]. This technique
197 has been used in previous studies to estimate the lower hybrid frequency using only the
198 electron and ion gyrofrequencies [Olsen *et al.*, 1987]. It only works under the approxima-
199 tion of dense plasma, otherwise it provides only an upper estimate of the lower hybrid
200 frequency.

201
202 Figure 3 shows strong diurnal variation in the frequency band above the 6th harmonic
203 of H^+ cyclotron frequency (silver line). The frequencies which show dayside enhancement

204 extend from 150 Hz to 600 Hz. Figure 3B highlights the change in power spectral den-
205 sity with MLT in this range of frequencies with a peak in the morning sector and the
206 lowest values occurring across the night side. This frequency band includes equatorial
207 noise/plasmaspheric hiss. The diurnal variation in plasmaspheric hiss is attributed to
208 keV electron injection into the outer plasmasphere on the dayside in conjunction with
209 substorms and to whistler-mode chorus, which is known to be a source of plasmaspheric
210 hiss, which can not propagate into the plasmasphere on the nightside due to stronger Lan-
211 dau damping caused by higher suprathermal electron flux [*Bortnik et al.*, 2007; *Li et al.*,
212 2013; *Chen et al.*, 2014; *Li et al.*, 2015]. Diurnal variation is also common in equatorial
213 noise and proton ring distributions can provide a source of free energy ring velocity (+/- a
214 factor of 2 above or below the Alfvénic speed) and generate equatorial noise [*Chen et al.*,
215 2010, 2011; *Hrbáčková et al.*, 2015].

216
217 Figure 4 highlights the power spectral densities for frequencies below 1000 Hz. Using
218 data from February 2013 to April 2015, EMFISIS WFR frequency channels were binned
219 by 0.25 L-Shell and 0.5 MLT for quiet times when $K_p < 3$. We did not set a limit on the
220 satellite's magnetic latitude in Figure 4. The wave amplitudes peak beyond 150 Hz, with
221 a dayside maximum at all L-Shells beginning at $f = 200$ Hz and continuing through $f =$
222 300 Hz. At 1000 Hz, the strong diurnal variation is absent, with a minimum at $L < 3$
223 dayside MLTs.

3. Quantitative Relationship Between Wave Amplitude and Low Energy Ions

225 In this section, we show how the Van Allen Probes observations dovetail with a reso-
226 nant interaction occurring between low energy ions and 150 Hz - 600 Hz waves. Figure 5
227 compares the median wave power spectral densities at harmonics of the H^+ cyclotron
228 frequency with median H^+ 1-10 eV partial densities at all MLTs for different L-Shells
229 from February 2013 to April 2015. Figure 5A shows $L = 2.0$, Figure 5B shows $L = 2.5$,
230 and Figure 5C shows $L = 3.0$. For each 4 second measurement of the magnetic field, the
231 gyrofrequency and harmonics of the gyrofrequency were calculated and then the electric
232 field power spectral density at the nearest frequency to the gyrofrequency was extracted
233 and binned.

234
235 The partial density and wave power spectral density behave differently at each of the
236 L-Shells. At $L = 2.0$, The 6th and 10th harmonic wave power spectral density begin to
237 decline at $MLT = 14$, dropping to approximately $10^{-12} V^2/m^2/Hz$ between $MLT = 19$ to
238 $MLT = 24$. The wave power spectral densities increase in three stages at $MLT = 4, 6,$ and
239 10 before reaching approximately $10^{-11} V^2/m^2/Hz$ across the dayside. The 16th harmonic
240 wave power spectral density is largely flat with little diurnal variation. The 1-10 eV H^+
241 density has a maximum at $MLT = 6$, beginning to increase at approximately $MLT = 4$.
242 The density gains and losses do not precisely follow the power spectral densities, but both
243 exhibit general diurnal variation.

244
245 For $L = 2.5$, the 6th, 10th, and 16th harmonic power spectral densities show the most
246 diurnal variation, varying between approximately $10^{-11} V^2/m^2/Hz$ from $MLT = 6$ to

247 MLT = 16 and approximately 10^{-12} V²/ m²/Hz from MLT = 17 to MLT = 3. The
248 different harmonic power spectral densities also follow each other closely with very sim-
249 ilar power spectral densities at different MLTs. The partial density also shows the most
250 diurnal variation of the three L-Shells shown, peaking from MLT = 6 to MLT = 22. The
251 rise of the 10th and 16th harmonics of the H⁺ gyrofrequency occur before the rise in the
252 partial density, although the peak power spectral density occurs after the partial density
253 has risen above 10^1 cm⁻³.

254
255 The L = 3.0 panel shows the least diurnal variation of the 6th, 10th, and 16th harmonic
256 power spectral densities. The heightened dayside power spectral densities occur from
257 MLT = 6 to MLT = 14 and the nightside low extends from MLT = 20 to MLT = 3. The
258 16th harmonic is strongest at this L-Shell, whereas the 6th and 10th harmonic are much
259 lower. The 1-10 eV density takes much longer to reach the high dayside values at this L-
260 Shell, not reaching peak value until MLT = 9 after a gradual increase starting at MLT = 1.

261
262 There are many factors contributing to the partial density increases in Figure 5. It
263 is important to note that harmonic cyclotron resonance occurs at multiple frequencies
264 and heats the ions differently based on the degree of the harmonic and the background
265 magnetic field conditions [*Schmitt, 1976; Mauk et al., 1981*]. So, in considering how power
266 spectral densities at different harmonics affect the 1-10 eV H⁺ partial densities across
267 MLTs, a holistic approach should be taken. For example, at L = 2.5 where all the power
268 spectral densities are high, the cumulative heating impact on the 1-10 eV ions from equa-
269 torial noise will be greater than at L = 3.0 where the 16th harmonic has a higher power

270 spectral density dayside value than the other harmonics. Also, at L-Shells closer to Earth,
271 the ionospheric contribution is greater and topside ionospheric plasma is transported into
272 the equatorial plasmasphere faster.

273
274 We developed a binary contingency table test to quantify if there was a connection
275 between waves with power spectral density above a certain level and high H⁺ fluxes.
276 Figure 6 shows the outcome of our threshold test. Each panel of Figure 6 shows the
277 percentage of each contingency table element based on MLT and L-Shell location. The
278 grid is divided into 0.25 L-Shell bins between 1.5 and 4 and 0.5 MLT bins between 0 and
279 24. The threshold bars were $10^8 \text{ cm}^{-2} \text{ s}^{-1} \text{ sr}^{-1} \text{ keV}^{-1}$ for H⁺ 2.5 eV fluxes and 10^{-12}
280 $\text{V}^2/\text{m}^2/\text{Hz}$ for EMFISIS power spectral densities at 250 Hz. The power spectral density
281 boundary is based on the electric field power spectral densities necessary for observable
282 transverse heating of a few eV per hour in the $2 < L < 3$ region [*Singh and Hwang, 1987*].
283 The flux threshold is based on measured HOPE fluxes at all MLTs for this energy channel.

284
285 The High Wave and Particle category denotes HOPE H⁺ fluxes of $10^8 \text{ cm}^{-2} \text{ s}^{-1} \text{ sr}^{-1}$
286 keV^{-1} or greater and a power spectral density of $10^{-12} \text{ V}^2/\text{m}^2/\text{Hz}$ or greater. The Low
287 Wave and Particle section denotes ion fluxes less than $10^8 \text{ cm}^{-2} \text{ s}^{-1} \text{ sr}^{-1} \text{ keV}^{-1}$ and power
288 spectral densities less than $10^{-12} \text{ V}^2/\text{m}^2/\text{Hz}$. Only High Wave occurs where the power
289 spectral densities are greater than $10^{-12} \text{ V}^2/\text{m}^2/\text{Hz}$ but the ion fluxes are less than 10^8
290 $\text{cm}^{-2} \text{ s}^{-1} \text{ sr}^{-1} \text{ keV}^{-1}$. Only High Particle occurs when power spectral densities are less
291 than $10^{-12} \text{ V}^2/\text{m}^2/\text{Hz}$ and the ion fluxes are greater than $10^8 \text{ cm}^{-2} \text{ s}^{-1} \text{ sr}^{-1} \text{ keV}^{-1}$.

293 There are several key ideas that emerge from Figure 6. When ion fluxes on the dayside
294 are high, in most cases between L-Shells of 1.5 to 3.25 and MLTs between 5 and 20,
295 the EMFISIS power spectral densities will be high and vice versa. This relationship is
296 demonstrated by the High Wave and Particle contingency outcome, where high percent-
297 ages ($> 70\%$) are seen in these L-Shell/MLT bins. On the other hand, the Low Wave
298 and Particle category shows us that in the post-midnight region between 0-5 MLT and
299 1.5 to 3.5 L-Shell, the opposite is seen with approximately equal occurrence frequency;
300 low ion fluxes are accompanied by low power spectral densities.

301
302 The Only High Particle and Only High Wave outcomes of the threshold test reveal
303 the areas subject to extenuating factors. The Only High Wave, where ion fluxes are low
304 despite high power spectral densities, occurs at higher L-Shells across many MLTs. We
305 attribute this largely to the declining ion densities from the conservation of the second
306 adiabatic invariant at higher L-Shells, so the threshold of $10^8 \text{ cm}^{-2} \text{ s}^{-1} \text{ sr}^{-1} \text{ keV}^{-1}$ is no
307 longer a strict threshold mark at $L > 3$. The Only High Particle outcome, where power
308 spectral densities are low but the particle fluxes are high, occurs at high percentages for
309 low L-Shells at MLTs of 5 to 20 and at higher L-Shells around $\text{MLT} = 18$. We attribute
310 this effect to ionospheric influence. From this binary contingency table, we can see that
311 there is a clear connection between wave amplitudes and high H^+ fluxes.

312
313 We supplement this statistical result with a case study to show the relationship between
314 dayside 1-10 eV H^+ flux enhancement and high wave amplitudes. Figure 7 highlights from
315 9:00-11:30 UT on July 2, 2013, when the Van Allen Probes A crossed the post-midnight

316 sector between $2 < L < 3$ on the outbound leg of the orbit. Figure 7A shows the EMFISIS
317 frequency spectrogram for the electric field component of the waves over the same time
318 period between 100 and 800 Hz. Figure 7B is the singular value decomposition (SVD)
319 ellipticity based on the magnetic component of the 250 Hz waves during this time period
320 [Santolik *et al.*, 2003]. The ellipticity indicates the polarization of the wave, with -1 as a
321 left hand polarized wave, 1 as a right hand polarized wave, and 0 as a linearly polarized
322 wave. Figure 7C is the pitch angle spectrogram from HOPE for the 3.38 eV energy chan-
323 nel. The black line is the 250 Hz power spectral density. In all of the panels, the orange
324 dotted lines highlight the post-midnight sector between $2 < L < 3$ and the pink dotted
325 lines highlight the $2 < L < 3$ afternoon ($15 < \text{MLT} < 18$) sector.

326
327 From the panels in Figure 7, there is an enhanced population around $\text{PA} = 90^\circ$ between
328 10:25 - 11:30 UT. At this same time, there are enhanced power spectral densities at or
329 near the sixth harmonic of the H^+ cyclotron frequency. The waves in the equatorial noise
330 frequency range, however, are primarily right hand polarized, indicating plasmaspheric
331 hiss. In the post-midnight sector, there is also an absence of high power spectral densities
332 and the pitch angle spectrograms reveal a relative minima in the $\text{PA} = 90^\circ$ population in
333 this region. The overall fluxes in the 3.38 eV energy range are severely depleted between
334 9:00 - 9:45 UT compared to the 10:25 - 11:30 UT 3.38 eV fluxes.

335
336 Figure 7C also shows relatively low 250 Hz power spectral densities in the post-midnight
337 sector compared to the inbound orbit power spectral densities and a near constant refilling
338 population from the 0° and 180° pitch angle fluxes. This case study shows an example of

339 nightside observations of low power spectral densities paired with little to no PA = 90°
340 H⁺ population, as well as dayside observations when both of these values are high. This
341 provides additional evidence supporting the idea that plasma waves could be heating the
342 low energy ions. This theory is supported by previous results in the literature [*Curtis*,
343 1985; *Okuma et al.*, 1987; *Singh and Hwang*, 1987; *Horne et al.*, 2000].

4. Polarization Reveals It's Mostly Plasmaspheric Hiss

345 However, there is conclusive evidence that these waves between 150 and 600 Hz at 2
346 $< L < 3$ with large power spectral densities are plasmaspheric hiss. Figure 8 shows the
347 median magnetic field ellipticity of 614 days of available data from both Van Allen Probes
348 A and B (double counting, so approximately 307 unique days from each satellite) between
349 February 2013 and April 2015 without distinguishing times of low/high Kp. Left Hand
350 waves are defined as having ellipticity < -0.2 , Right Hand waves as having ellipticity $>$
351 0.2 , and Linear Polarization as waves with ellipticity falling between -0.2 and 0.2 [*Santolík*
352 *et al.*, 2004; *Li et al.*, 2015]. We only take times where planarity > 0.5 . The dotted lines
353 highlight between 150 Hz and 600 Hz, where we see the peak wave amplitudes. Each
354 event is a 1-second measurement between $2 < L < 3$. Figure 8 shows that approximately
355 1% of the wave measurements between $2 < L < 3$ at frequencies of 150 to 600 Hz are
356 linearly polarized or left hand polarized.

357
358 Figure 9 shows the median polarization and power spectral density of right hand waves
359 versus linearly polarized waves at $L = 2.5$ at MLT = 3, 9, 15, and 21 from February 2013
360 to April 2015 at times where Kp < 3 . The top panel shows the median polarization, or

361 the ellipticity without sense of direction, of all the waves between 0 and 90 degrees. The
362 middle panel shows the power spectral density of waves with polarization greater than
363 0.7, which we know from case studies and Figure 8 are right hand polarized waves. They
364 could be left hand polarized waves since our SVD polarization algorithm can only differ-
365 entiate between circular and linearly polarized without offering information direction like
366 the limited EMFISIS L4 files can. However, Figure 8 confirms that 99% of measurements
367 are right-hand polarized between 150 - 600 Hz, and Figure 9 contains analyzed data from
368 every day between February 2013 and April 2015 and was screened based on the Kp index.
369 The lowest panel shows the linearly polarized waves with polarization < 0.2 . The dotted
370 lines highlight between 150 Hz and 600 Hz.

371
372 From Figure 8 and Figure 9, we know waves that show high occurrence probability with
373 elevated 1-10 eV populations levels are right hand polarized waves which would not be
374 cyclotron resonant with ions of these energies. Anomalous resonance between the ions and
375 plasmaspheric hiss was considered, as described by *Tsurutani and Lakhina [1997]; Tsur-*
376 *rutani et al. [1998]; Kozyra et al. [1994, 1995]*. However, anomalous resonance requires
377 that the phase velocity of the wave is smaller than the particle parallel velocity, which
378 is in contradiction with our extremely low energy ions with near $PA = 90^\circ$ and reason-
379 able k vector magnitudes in the inner magnetosphere of 10^{-3} m^{-1} [*Walker et al., 2015*].
380 Therefore, right hand plasmaspheric hiss, despite evidence in Figure 6 and suggestion in
381 previous work [*Curtis, 1985; Olsen et al., 1987; Singh and Hwang, 1987; Horne et al.,*
382 *2000*], is not responsible for the variation in the suprathermal 1-10 eV ion population.
383 Underlying left hand or linearly polarized components of plasmaspheric hiss, however,

could be responsible for the ion heating, which will be explored in a follow-up study.

5. Conclusions

We have demonstrated that the 1-10 eV H^+ ions measured by the Van Allen Probes exhibit strong diurnal variation in flux measurements with pitch angles near 90° . In particular, this effect is prominent in lower energy particles as seen in Figure 2. Also, when examining pitch angle fluxes against energy, the low energy fluxes at near $PA = 90^\circ$ rise first and then the higher energy equatorially mirroring H^+ fluxes increase in Figure 1. With these factors combined, the depletion of ions described in [Sarno-Smith et al., 2015] is not actually a loss or a transport effect - it is the result of low energy ion heating across the dayside, likely due to wave-particle interactions.

We then demonstrated a possible cause for the 1-10 eV ion heating across the dayside - higher order cyclotron resonance. Enhanced levels of polarized plasma waves between the ion cyclotron frequency and lower hybrid frequency at $2 < L < 3$ showed similar statistical rises and falls as the 1-10 eV ions in this same region. The binary contingency tables demonstrated that times where waves had amplitudes above $10^{-11} \text{ V}^2/\text{m}^2/\text{Hz}$ aligned well with times of high low energy ions fluxes. In more than 70% of cases on the dayside at $2 < L < 3$, high power spectral density waves occurred with high particle fluxes. In the post-midnight sector, over 70% of the instances had low power spectral densities and low particle fluxes below $L < 3$.

405 To further solidify this relationship, a case study was presented where high power spec-
406 tral densities at 250 Hz occurred when HOPE measured high PA near 90° populations.
407 In the post-midnight sector, this case study showed that the equatorially mirroring popu-
408 lation was at a relative minimum while the 0° and 180° pitch angle bins were at a relative
409 maximum. However, this case study also highlights that these high power spectral den-
410 sity waves on the dayside at $2 < L < 3$ are right hand polarized plasmaspheric hiss not
411 linearly polarized equatorial noise. Figures 8 and 9 confirm that the 150 - 600 Hz waves
412 that exhibit similar diurnal variation to the 1-10 eV ion fluxes are right hand polarized
413 approximately 99% of the time and would not cyclotron resonate with the 1-10 eV ions.
414

415 Open questions still remain. Previous studies connected suprathermal ions with the
416 presence of high power spectral density equatorial noise in the equatorial plane; however,
417 the polarization analysis performed in our study reveals that these waves between $2 <$
418 $L < 3$ are primarily plasmaspheric hiss. Nevertheless, the binary contingency table in
419 Figure 6 demonstrated a connection between the 1-10 eV H^+ fluxes and plasmaspheric
420 hiss, so there may be a third variable affecting both plasmaspheric hiss presence and 1-10
421 eV H^+ energization on the inner plasmasphere dayside. The potential heating of He^+ and
422 O^+ has not been examined in regards to a connection with plasmaspheric hiss. Also the
423 low energy electrons (< 500 eV) have not been examined in the Van Allen Probes dataset
424 yet in regards to wave activity or in relation to fluctuations in the low energy 1-10 eV
425 population, similar to the findings of *Knudsen et al.* [1998]. Our study concludes that
426 contrary to prior evidence [*Curtis*, 1985; *Olsen et al.*, 1987; *Singh and Hwang*, 1987; *Horne*
427 *et al.*, 2000], large power spectral density right hand waves with frequencies between 150

428 Hz and 600 Hz in the near-Earth equatorial plane do not interact with the 1-10 eV ion
429 population although they exhibit similar diurnal variation.

430

431 **Acknowledgments.** The Michigan co-authors would like to thank the University of
432 Michigan Rackham Graduate school, NASA, and the NSF for sponsoring this work under
433 grants NNX11A060G, NNX144AC02G, AGS-1265651, and AGS-1102863. Work at Los
434 Alamos National Laboratory was performed under the auspices of the U.S. Department of
435 Energy, with support from the NASA Van Allen Probes mission under interagency transfer
436 NNG07EK091 and approved for public release as LA-UR-16-25767. The research at The
437 University of Iowa was supported by JHU/APL contract no. 921647. Data from HOPE
438 and EMFISIS used to generate figures for this project came from the Van Allen Probes
439 data center at <https://emfisis.physics.uiowa.edu/data/index> and <http://rbsp-ect.lanl.gov/>

References

440 Boardsen, S. A., G. B. Hospodarsky, C. A. Kletzing, M. J. Engebretson, R. F. Pfaff,
441 J. R. Wiggant, W. S. Kurth, T. F. Averkamp, S. R. Bounds, J. L. Green, et al. (2016),
442 Survey of the frequency dependent latitudinal distribution of the fast magnetosonic
443 wave mode from van allen probes electric and magnetic field instrument and integrated
444 science waveform receiver plasma wave analysis, *Journal of Geophysical Research: Space*
445 *Physics*.

446 Bortnik, J., B. Thorne, and N. Meredith (2007), Modeling the propagation characteristics
447 of chorus using crres suprathermal electron fluxes, *Journal of Geophysical Research:*
448 *Space Physics*, 112(A8).

- 449 Bortnik, J., R. M. Thorne, and N. P. Meredith (2008), The unexpected origin of plasma-
450 spheric hiss from discrete chorus emissions, *Nature*, *452*(7183), 62–66.
- 451 Chen, L., R. M. Thorne, V. K. Jordanova, and R. B. Horne (2010), Global simulation of
452 magnetosonic wave instability in the storm time magnetosphere, *Journal of Geophysical
453 Research: Space Physics*, *115*(A11), n/a–n/a, doi:10.1029/2010JA015707, a11222.
- 454 Chen, L., R. M. Thorne, V. K. Jordanova, M. F. Thomsen, and R. B. Horne (2011),
455 Magnetosonic wave instability analysis for proton ring distributions observed by the
456 lanl magnetospheric plasma analyzer, *Journal of Geophysical Research: Space Physics*,
457 *116*(A3).
- 458 Chen, L., R. M. Thorne, J. Bortnik, W. Li, R. B. Horne, G. D. Reeves, C. A. Kletzing,
459 W. S. Kurth, G. B. Hospodarsky, H. E. Spence, J. B. Blake, and J. F. Fennell (2014),
460 Generation of unusually low frequency plasmaspheric hiss, *Geophysical Research Letters*,
461 *41*(16), 5702–5709, doi:10.1002/2014GL060628.
- 462 Church, S., and R. M. Thorne (1983), On the origin of plasmaspheric hiss: Ray path
463 integrated amplification, *Journal of Geophysical Research: Space Physics*, *88*(A10),
464 7941–7957.
- 465 Curtis, S. (1985), Equatorial trapped plasmasphere ion distributions and transverse
466 stochastic acceleration, *Journal of Geophysical Research: Space Physics (1978–2012)*,
467 *90*(A2), 1765–1770.
- 468 Draganov, A., U. Inan, V. Sonwalkar, and T. Bell (1992), Magnetospherically reflected
469 whistlers as a source of plasmaspheric hiss, *Geophysical research letters*, *19*(3), 233–236.
- 470 Funsten, H., B. Skoug, A. Guthrie, E. MacDonald, J. Baldonado, R. Harper, K. Hender-
471 son, K. Kihara, J. Lake, B. Larsen, et al. (2014), Helium, oxygen, proton, and electron

- 472 (hope) mass spectrometer for the radiation belt storm probes mission, in *The Van Allen*
473 *Probes Mission*, pp. 423–484, Springer.
- 474 Gary, S. P., K. Liu, D. Winske, and R. E. Denton (2010), Ion Bernstein instability in the
475 terrestrial magnetosphere: Linear dispersion theory, *Journal of Geophysical Research:*
476 *Space Physics (1978–2012)*, 115(A12).
- 477 Green, J. L., S. F. Fung, S. Boardsen, and H. J. Christian (2005), Distribution and origin
478 of plasmaspheric plasma waves, *Inner Magnetosphere Interactions: New Perspectives*
479 *from Imaging*, pp. 113–126.
- 480 Gurnett, D. A. (1976), Plasma wave interactions with energetic ions near the magnetic
481 equator, *Journal of Geophysical Research*, 81(16), 2765–2770.
- 482 Horne, R. B., G. V. Wheeler, and H. S. C. Alleyne (2000), Proton and electron heating by
483 radially propagating fast magnetosonic waves, *Journal of Geophysical Research: Space*
484 *Physics (1978–2012)*, 105(A12), 27,597–27,610.
- 485 Hrbáčková, Z., O. Santolík, F. Němec, E. Macušová, and N. Cornilleau-Wehrin (2015),
486 Systematic analysis of occurrence of equatorial noise emissions using 10 years of data
487 from the cluster mission, *Journal of Geophysical Research: Space Physics*, 120(2), 1007–
488 1021.
- 489 Kletzing, C. W., W. Kurth, M. Acuna, R. MacDowall, R. Torbert, T. Averkamp, D. Bodet,
490 S. Bounds, M. Chutter, J. Connerney, et al. (2014), The electric and magnetic field
491 instrument suite and integrated science (emfis) on rbsp, in *The Van Allen Probes*
492 *Mission*, pp. 127–181, Springer.
- 493 Knudsen, D. J., J. H. Clemmons, and J.-E. Wahlund (1998), Correlation between core ion
494 energization, suprathermal electron bursts, and broadband ELF plasma waves, *Journal*

- 495 *of Geophysical Research: Space Physics*, 103(A3), 4171–4186.
- 496 Kozyra, J., C. Rasmussen, R. Miller, and L. Lyons (1994), Interaction of ring current
497 and radiation belt protons with ducted plasmaspheric hiss: 1. diffusion coefficients and
498 timescales, *Journal of Geophysical Research: Space Physics*, 99(A3), 4069–4084.
- 499 Kozyra, J., C. Rasmussen, R. Miller, and E. Villalon (1995), Interaction of ring cur-
500 rent and radiation belt protons with ducted plasmaspheric hiss: 2. time evolution of
501 the distribution function, *Journal of Geophysical Research: Space Physics*, 100(A11),
502 21,911–21,919.
- 503 Kurth, W., S. De Pascuale, J. Faden, C. Kletzing, G. Hospodarsky, S. Thaller, and
504 J. Wygant (2015), Electron densities inferred from plasma wave spectra obtained by
505 the waves instrument on van allen probes, *Journal of Geophysical Research: Space
506 Physics*, 120(2), 904–914.
- 507 Laakso, H., H. Junginger, A. Roux, R. Schmidt, and C. d. Villedary (1990), Magnetosonic
508 waves above f_c ($h+$) at geostationary orbit: Geos 2 results, *Journal of Geophysical
509 Research: Space Physics (1978–2012)*, 95(A7), 10,609–10,621.
- 510 Lennartsson, W., and D. L. Reasoner (1978), Low-energy plasma observations at syn-
511 chronous orbit, *Journal of Geophysical Research: Space Physics (1978–2012)*, 83(A5),
512 2145–2156.
- 513 Li, W., Y. Snprits, and R. Thorne (2007), Dynamic evolution of energetic outer zone elec-
514 trons due to wave-particle interactions during storms, *Journal of Geophysical Research:
515 Space Physics*, 112(A10).
- 516 Li, W., R. M. Thorne, J. Bortnik, G. D. Reeves, C. A. Kletzing, W. S. Kurth, G. B.
517 Hospodarsky, H. E. Spence, J. B. Blake, J. F. Fennell, S. G. Claudepierre, J. R. Wygant,

- 518 and S. A. Thaller (2013), An unusual enhancement of low-frequency plasmaspheric
519 hiss in the outer plasmasphere associated with substorm-injected electrons, *Geophysical*
520 *Research Letters*, *40*(15), 3798–3803, doi:10.1002/grl.50787.
- 521 Li, W., Q. Ma, R. Thorne, J. Bortnik, C. Kletzing, W. Kurth, G. Hospodarsky, and
522 Y. Nishiyama (2015), Statistical properties of plasmaspheric hiss derived from van allen
523 probes data and their effects on radiation belt electron dynamics, *Journal of Geophysical*
524 *Research: Space Physics*, *120*(5), 3393–3405.
- 525 Ma, Q., W. Li, R. M. Thorne, and V. Angelopoulos (2013), Global distribution of equa-
526 torial magnetosonic waves observed by themis, *Geophysical Research Letters*, *40*(10),
527 1895–1901.
- 528 Ma, Q., W. Li, R. M. Thorne, J. Bortnik, C. Kletzing, W. Kurth, and G. Hospodarsky
529 (2016), Electron scattering by magnetosonic waves in the inner magnetosphere, *Journal*
530 *of Geophysical Research: Space Physics*, *121*(1), 274–285.
- 531 Mauk, B., C. Mclwain, and m. L. McPherron (1981), Helium cyclotron resonance within
532 the earth's magnetosphere, *Geophysical Research Letters*, *8*(1), 103–106.
- 533 Mauk, B., N. J. Fox, S. Kanekal, R. Kessel, D. Sibeck, and A. Ukhorskiy (2014), Science
534 objectives and rationale for the radiation belt storm probes mission, in *The Van Allen*
535 *Probes Mission*, pp. 3–27, Springer.
- 536 Meredith, N. P., R. B. Horne, S. A. Glauert, and R. R. Anderson (2007), Slot region
537 electron loss timescales due to plasmaspheric hiss and lightning-generated whistlers,
538 *Journal of Geophysical Research: Space Physics*, *112*(A8).
- 539 Meredith, N. P., R. B. Horne, and R. R. Anderson (2008), Survey of magnetosonic waves
540 and proton ring distributions in the earth's inner magnetosphere, *Journal of Geophysical*

- 541 *Research: Space Physics (1978–2012)*, 113(A6).
- 542 Meredith, N. P., R. B. Horne, S. A. Glauert, D. N. Baker, S. G. Kanekal, and J. M. Albert
543 (2009), Relativistic electron loss timescales in the slot region, *Journal of Geophysical*
544 *Research: Space Physics*, 114(A3).
- 545 Němec, F., O. Santolík, K. Gereová, E. Macušová, H. Laakso, Y. De Conchy, M. Mak-
546 simovic, and N. Cornilleau-Wehrin (2006), Equatorial noise: Statistical study of its
547 localization and the derived number density, *Advances in Space Research*, 37(3), 610–
548 616.
- 549 Němec, F., O. Santolík, Z. Hrbáčková, and N. Cornilleau-Wehrin (2015), Intensities and
550 spatiotemporal variability of equatorial noise emissions observed by the cluster space-
551 craft, *Journal of Geophysical Research: Space Physics*, 120(3), 1620–1632.
- 552 Olsen, R., S. Shawhan, D. Gallagher, J. Green, C. Chappell, and R. Anderson (1987),
553 Plasma observations at the earth’s magnetic equator, *Journal of Geophysical Research:*
554 *Space Physics (1978–2012)*, 92(A3), 2385–2407.
- 555 Perraut, S. (1982), Wave-particle interactions in the ulf range: Geos-1 and-2 results,
556 *Planetary and Space Science*, 30(12), 1219–1227.
- 557 Perraut, S., A. Roux, P. Robert, R. Gendrin, J.-A. Sauvaud, J.-M. Bosqued, G. Kremser,
558 and A. Korth (1982), A systematic study of ulf waves above fh+ from geos 1 and 2 mea-
559 surements and their relationships with proton ring distributions, *Journal of Geophysical*
560 *Research: Space Physics (1978–2012)*, 87(A8), 6219–6236.
- 561 Quinn, J., and R. Johnson (1982), Composition measurements of warm equatorially
562 trapped ions near geosynchronous orbit, *Geophysical Research Letters*, 9(7), 777–780.

- 563 Roux, A., S. Perraut, J. Rauch, C. Villedary, G. Kremser, A. Korth, and D. Young (1982),
564 Wave-particle interactions near ω_{he+} observed on board geos 1 and 2: 2. generation of
565 ion cyclotron waves and heating of he+ ions, *Journal of Geophysical Research: Space*
566 *Physics (1978–2012)*, *87*(A10), 8174–8190.
- 567 Russell, C. T., R. E. Holzer, and E. J. Smith (1970), Ogo 3 observations of elf noise in the
568 magnetosphere: 2. the nature of the equatorial noise, *Journal of Geophysical Research*,
569 *75*(4), 755–768.
- 570 Santolik, O., M. Parrot, L. Storey, J. Pickett, and D. Gurnett (2001), Propagation analysis
571 of plasmaspheric hiss using polar pwi measurements, *Geophysical research letters*, *28*(6),
572 1127–1130.
- 573 Santolik, O., J. Pickett, D. Gurnett, M. Maksimovic, and N. Cornilleau-Wehrin (2002),
574 Spatiotemporal variability and propagation of equatorial noise observed by cluster,
575 *Journal of Geophysical Research: Space Physics*, *107*(A12).
- 576 Santolik, O., M. Parrot, and F. Lefeuvre (2003), Singular value decomposition methods
577 for wave propagation analysis, *Radio Science*, *38*(1).
- 578 Santolik, O., F. Nemeč, K. Gereová, E. Macúšová, Y. De Conchy, and N. Cornilleau-
579 Wehrin (2004), Systematic analysis of equatorial noise below the lower hybrid fre-
580 quency, in *Annales Geophysicae*, vol. 22, pp. 2587–2595.
- 581 Sarno-Smith, L. K., M. W. Liemohn, R. M. Katus, R. M. Skoug, B. A. Larsen, M. F.
582 Thomsen, J. R. Wygant, and M. B. Moldwin (2015), Postmidnight depletion of the
583 high-energy tail of the quiet plasmasphere, *Journal of Geophysical Research: Space*
584 *Physics*, *120*(3), 1646–1660.

- 585 Sarno-Smith, L. K., M. W. Liemohn, R. M. Skoug, B. A. Larsen, M. B. Moldwin, R. M.
586 Katus, and J. R. Wygant (2016a), Local time variations of high-energy plasmaspheric
587 ion pitch angle distributions, *Journal of Geophysical Research: Space Physics*.
- 588 Sarno-Smith, L. K., B. A. Larsen, R. M. Skoug, M. W. Liemohn, A. Breneman, J. R.
589 Wygant, and M. F. Thomsen (2016b), Spacecraft surface charging within geosyn-
590 chronous orbit observed by the van allen probes, *Space Weather*, *14*(2), 151–164, doi:
591 10.1002/2015SW001345, 2015SW001345.
- 592 Schmitt, J. (1976), Nonlinear theory of rf heating at cyclotron harmonics, *Physics of*
593 *Fluids (1958-1988)*, *19*(2), 245–255.
- 594 Singh, N., and K. Hwang (1987), Perpendicular ion heating effects on the refilling of
595 the outer plasmasphere, *Journal of Geophysical Research: Space Physics (1978–2012)*,
596 *92*(A12), 13,513–13,521.
- 597 Solomon, J., N. Cornilleau-Wehrin, A. Korth, and G. Kremser (1988), An experimental
598 study of elf/vlf hiss generation in the earth's magnetosphere, *Journal of Geophysical*
599 *Research: Space Physics*, *93*(A3), 1839–1847.
- 600 Summers, D., B. Ni, and N. P. Meredith (2007), Timescales for radiation belt electron
601 acceleration and loss due to resonant wave-particle interactions: 2. evaluation for vlf
602 chorus, elf hiss, and electromagnetic ion cyclotron waves, *Journal of Geophysical Re-*
603 *search: Space Physics*, *112*(A4).
- 604 Thorne, R. M., and J. N. Barfield (1976), Further observational evidence regarding the
605 origin of plasmaspheric hiss, *Geophysical Research Letters*, *3*(1), 29–32.
- 606 Thorne, R. M., E. J. Smith, R. K. Burton, and R. E. Holzer (1973), Plasmaspheric hiss,
607 *Journal of Geophysical Research*, *78*(10), 1581–1596.

- 608 Tsurutani, B., J. Arballo, G. Lakhina, C. Ho, B. Buti, J. Pickett, and D. Gurnett (1998),
609 Plasma waves in the dayside polar cap boundary layer: Bipolar and monopolar electric
610 pulses and whistler mode waves, *Geophysical research letters*, *25*(22), 4117–4120.
- 611 Tsurutani, B. T., and G. S. Lakhina (1997), Some basic concepts of wave-particle inter-
612 action in collisionless plasmas, *Reviews of Geophysics*, *35*(4), 491–501.
- 613 Tsurutani, B. T., E. J. Smith, and R. M. Thorne (1975), Electromagnetic hiss and rela-
614 tivistic electron losses in the inner zone, *Journal of Geophysical Research*, *80*(4), 600–
615 607.
- 616 Walker, S., M. Balikhin, D. Shklyar, K. Yearby, P. Canu, C. Carr, and I. Dandouras
617 (2015), Experimental determination of the dispersion relation of magnetosonic waves,
618 *Journal of Geophysical Research: Space Physics*, *120*(11), 9632–9650.
- 619 Wygant, J. I. Bonnell, K. Goetz, R. Ergun, F. Mozer, S. Bale, M. Ludlam, P. Turin,
620 P. Harvey, R. Hochmann, et al. (2013), The electric field and waves instruments on the
621 radiation belt storm probes mission, *Space Science Reviews*, *179*(1-4), 183–220.
- 622 Young, D., S. Perraut, A. Roux, C. Villedary, R. Gendrin, A. Korth, G. Kremser, and
623 D. Jones (1981), Wave-particle interactions near ω_{he+} observed on geos 1 and 2 1.
624 propagation of ion cyclotron waves in he+-rich plasma, *Journal of Geophysical Research:*
625 *Space Physics (1978–2012)*, *86*(A8), 6755–6772.

Figure 1. Median differential number fluxes corrected for spacecraft potential for 1.5-10 eV H^+ measured by HOPE at $L = 2.5$ at several MLTs from February 2013 to April 2015. The fluxes were binned by energy channel and pitch angle.

Figure 2. Normalized median differential number fluxes corrected for spacecraft potential for 1.5 eV, 1.83 eV, 2.18 eV, 2.53 eV, 2.95 eV, 3.38 eV, 3.94 eV, 4.64 eV and 5.35 eV H^+ measured by HOPE at $L = 2.5$ from February 2013 to April 2015 for $PA=18^\circ, 54^\circ, 90^\circ, 144^\circ,$ and 162° . The median fluxes were normalized based on the maximum value for each energy at all MLTs.

Figure 3. A shows the median power spectral density of the electric field component of waves measured from EMFISIS in 0.5 MLT bins and logarithmically spaced frequency bins between 10 Hz and 1 kHz over from February 2013 to April 2015 at $L=2.5$. B is the power spectral density of the electric field wave component normalized across all MLTs by the max value at each frequency/0.5 MLT bin over the same time period at $L=2.5$. In both A and B, the silver line is the 6th harmonic of the H^+ cyclotron frequency.

Figure 4. Median equatorial noise electric field power spectral densities at different frequency bands from EMFISIS. Each frequency band was sorted by 0.25 L-Shell and 0.5 MLT from February 2013 to April of 2015 at times when $Kp < 3$.

Figure 5. The blue, green, and gold lines are the median electric field power spectral density measured by EMFISIS from February 2013 to April 2015 for the 6th harmonic, 10th harmonic, and 16th harmonic of the H^+ gyrofrequency, approximately 100 - 250 Hz. The different panels show different L-Shells, with A at $L = 2.0$, B at $L = 2.5$, and C at $L = 3.0$. The dashed black line is the median H^+ partial 1-10 eV density over the same time period at the same L-Shell. Both the power spectral densities and H^+ partial densities were binned by 0.25 L-Shell and 0.5 MLT.

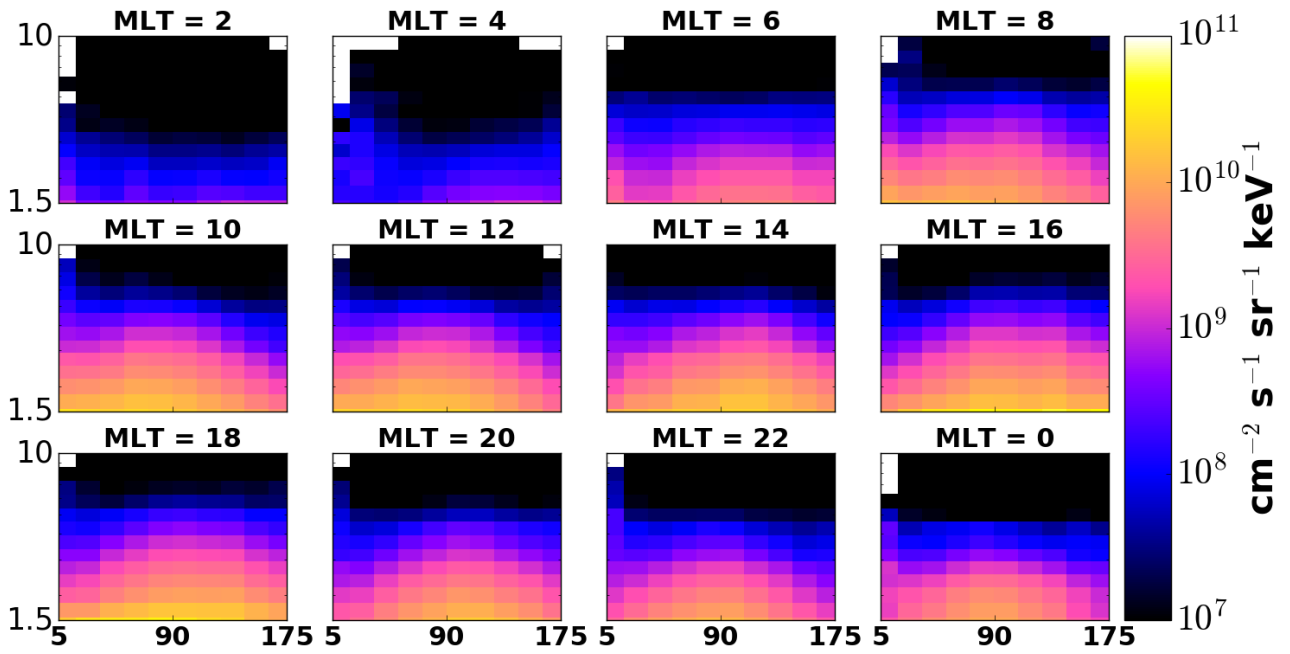
Figure 6. Binary contingency table results of median HOPE 2.5 eV fluxes and EMFISIS electric field power spectral densities at 250 Hz. The study used data from February 2013 to April 2015 which was sorted into 0.25 L-Shell and 0.5 MLT bins. The High Wave and Particle category denotes HOPE H⁺ fluxes of $10^8 \text{ cm}^{-2} \text{ s}^{-1} \text{ sr}^{-1} \text{ keV}^{-1}$ or greater and a power spectral density of $10^{-12} \text{ V}^2/\text{m}^2/\text{Hz}$ or greater. The Low Wave and Particle section denotes ion fluxes less than $10^8 \text{ cm}^{-2} \text{ s}^{-1} \text{ sr}^{-1} \text{ keV}^{-1}$ and power spectral densities less than $10^{-12} \text{ V}^2/\text{m}^2/\text{Hz}$. Only High Wave occurs where the power spectral densities are greater than $10^{-12} \text{ V}^2/\text{m}^2/\text{Hz}$ but the ion fluxes are less than $10^8 \text{ cm}^{-2} \text{ s}^{-1} \text{ sr}^{-1} \text{ keV}^{-1}$. Only High Particle occur when power spectral densities are less than $10^{-12} \text{ V}^2/\text{m}^2/\text{Hz}$ and the ion fluxes are greater than $10^8 \text{ cm}^{-2} \text{ s}^{-1} \text{ sr}^{-1} \text{ keV}^{-1}$. The color of each bin reflects the percentage of the bins that lie in each respective category.

Figure 7. Case study on July 2, 2013 from 9 to 11:30 UT with Van Allen Probes A data. Panel A is the EMFISIS WFR spectra between 100 to 700 Hz. Panel B is the ellipticity calculated using singular value decomposition, where +1 indicates right hand polarized waves, 0 is linearly polarized waves, and -1 is left hand polarized waves. Panel C is the H⁺ 3.38 eV energy channel differential number fluxes measured in each pitch angle bin over this time interval. The black line is 250 Hz power spectral density. In all panels, the orange dotted lines demarcate where $2 < L < 3$ where $1 < \text{MLT} < 4$ and the green dotted lines highlight where $2 < L < 3$ on the dayside between $15 < \text{MLT} < 18$.

Figure 8. Using 614 days of data from both RBSP-A and RBSP-B (double counting, so approximately 307 unique days), we use ellipticity to determine the sense of the waves in addition to the polarization. Left Hand waves are defined as having ellipticity < -0.2 , Right Hand waves as having ellipticity > 0.2 , and Linear Polarization as waves with ellipticity falling between -0.2 and 0.2 . The dotted lines highlight between 150 Hz and 600 Hz, where we see the peak wave amplitudes. Each event is a 1 second measurement between $2 < L < 3$.

Figure 9. These panels show the median polarization and power spectral density of right hand waves versus linearly polarized waves at $L = 2.5$ at $MLT = 3, 9, 15,$ and 21 from February 2013 to April 2015. The top panel shows the median polarization of all the waves between 0 and 90 degrees. The middle panel shows the power spectral density of waves with polarization greater than 0.7, which here we know from case studies are right hand polarized waves. The lowest panel shows the linearly polarized waves with polarization < 0.2 . The dotted lines highlight between 150 Hz and 600 Hz.

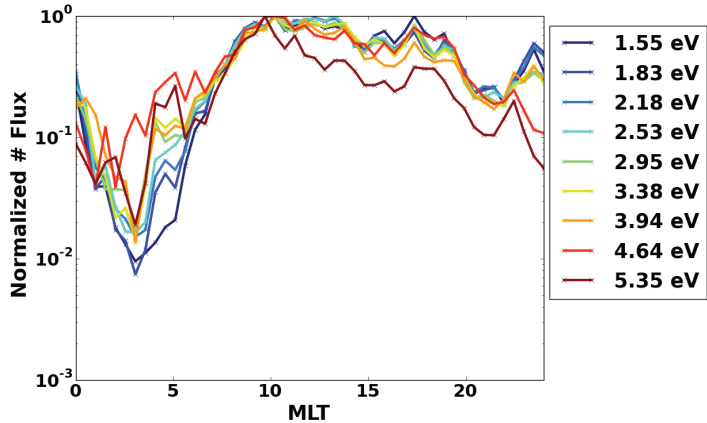
cript



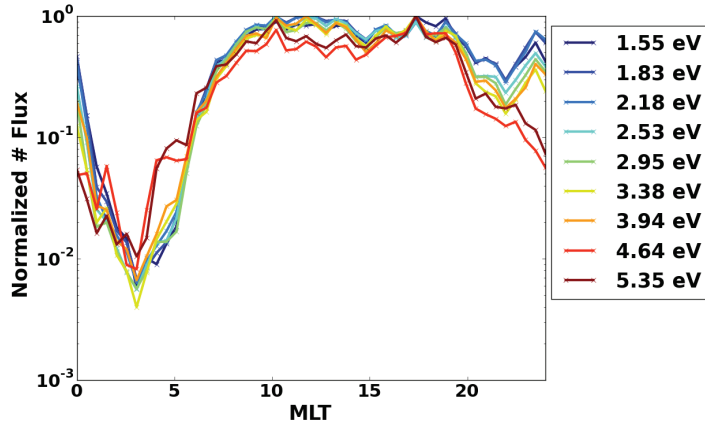
Autl

2016JA022975-f01-z.png

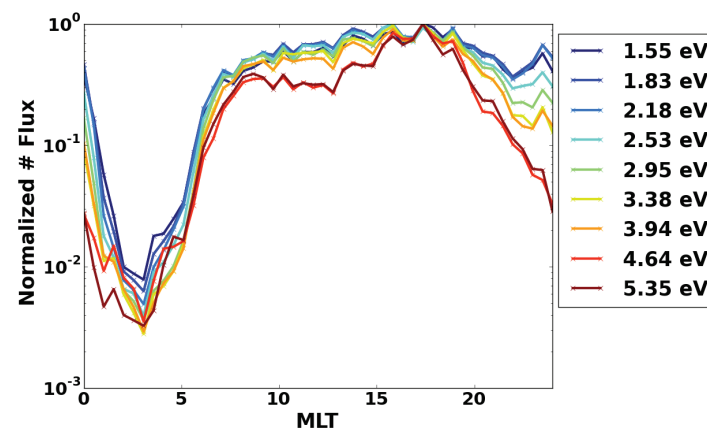
PA = 18°



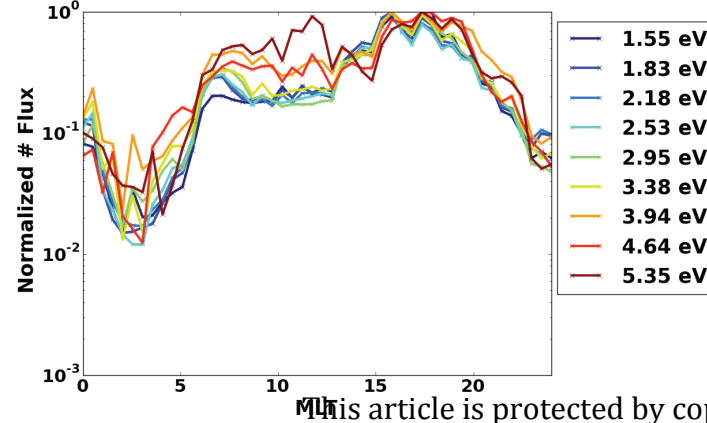
PA = 54°



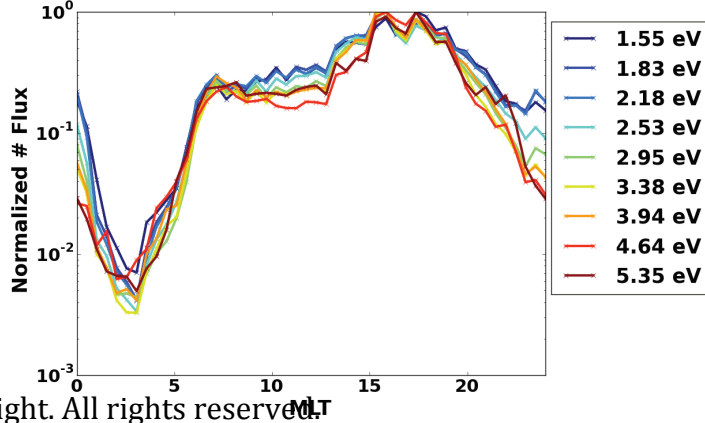
PA = 90°

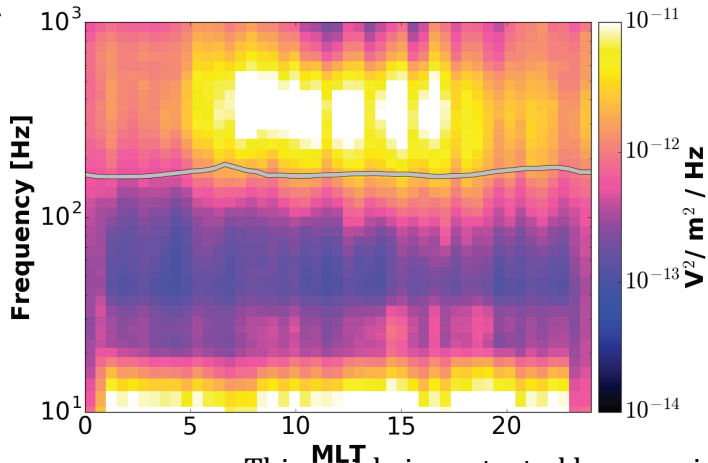
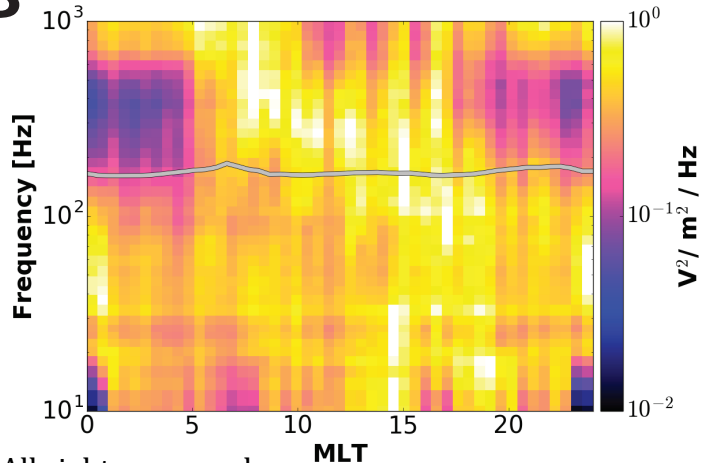


PA = 162°



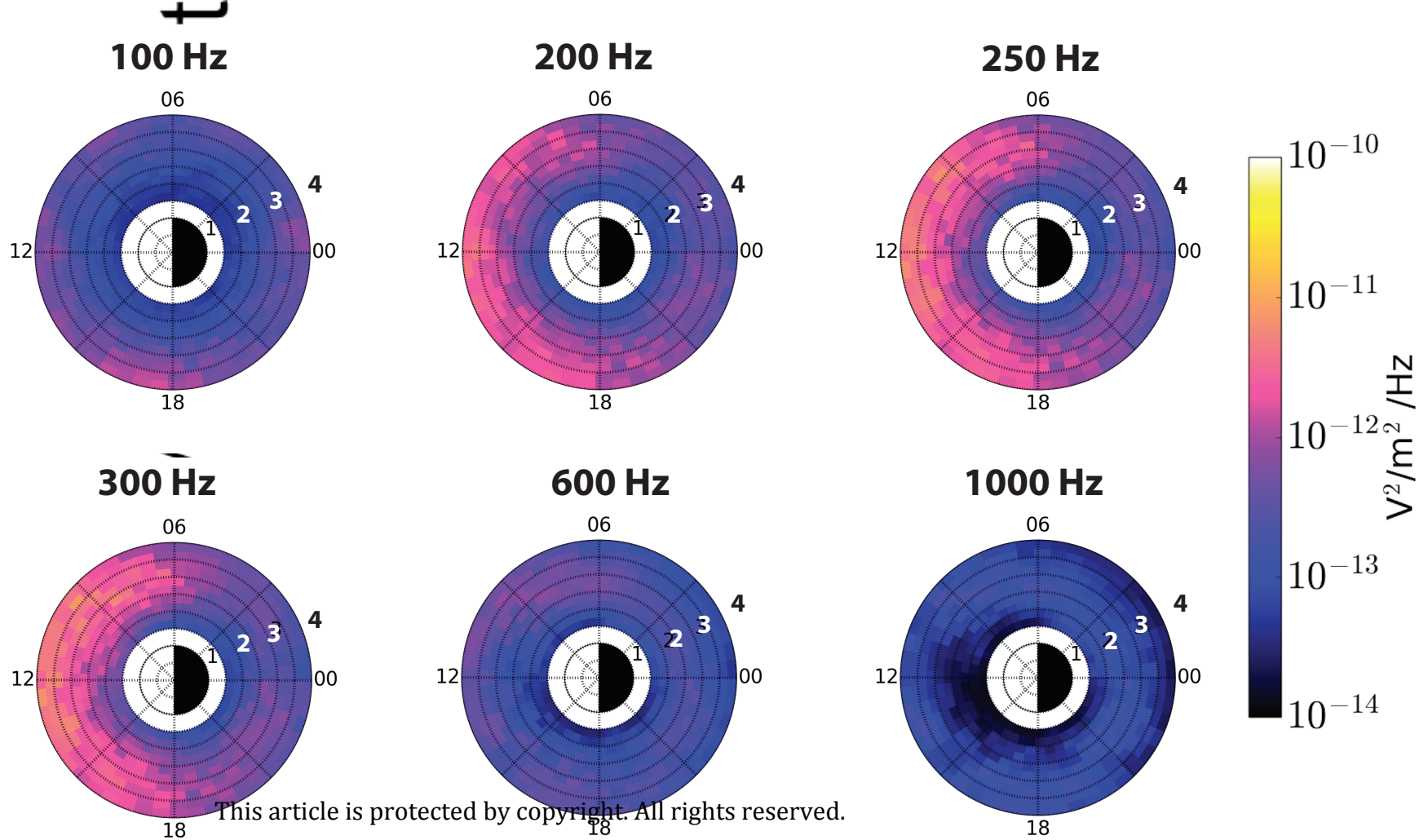
PA = 144°



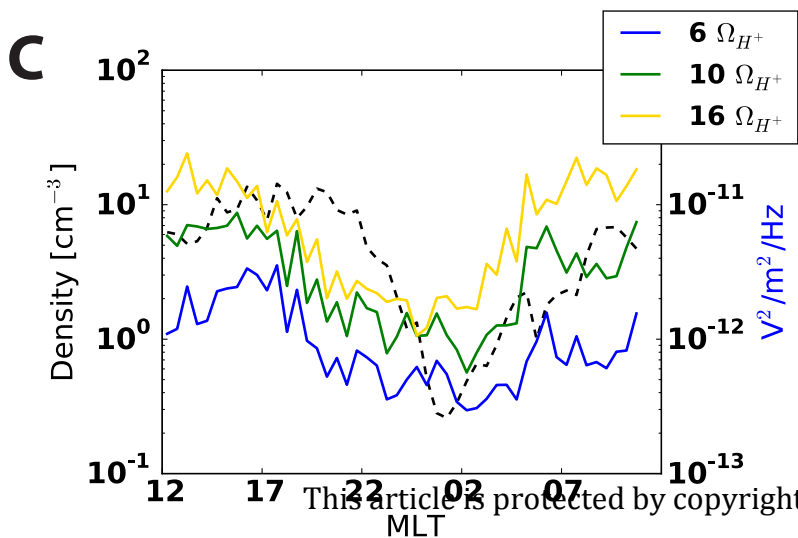
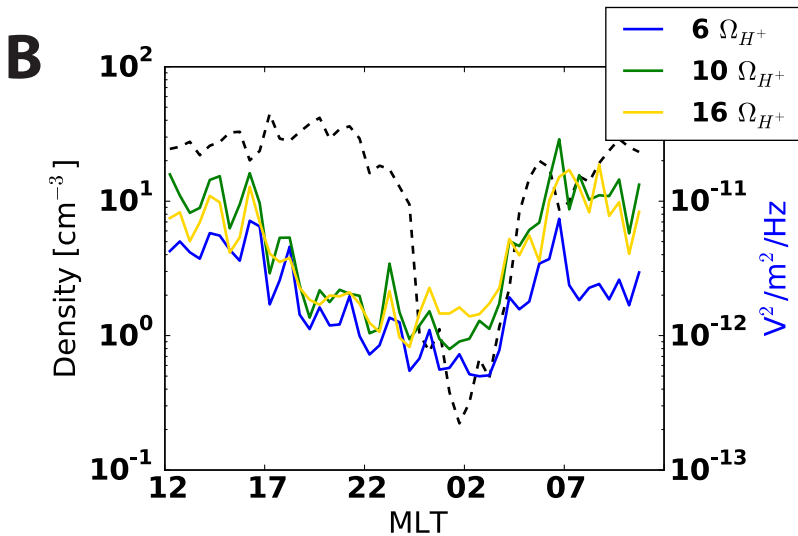
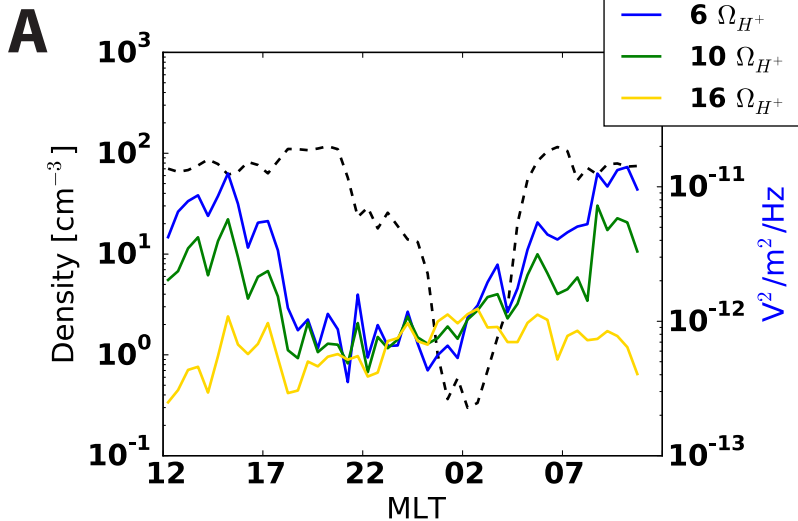
A**B**

This article is protected by copyright. All rights reserved.

A



This article is protected by copyright. All rights reserved.



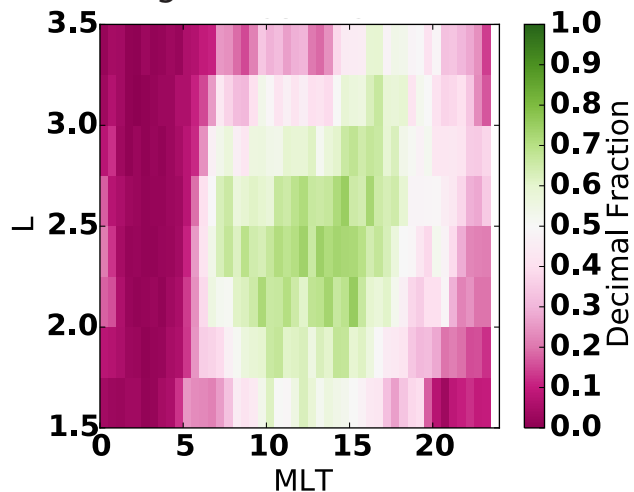
pt

High Wave

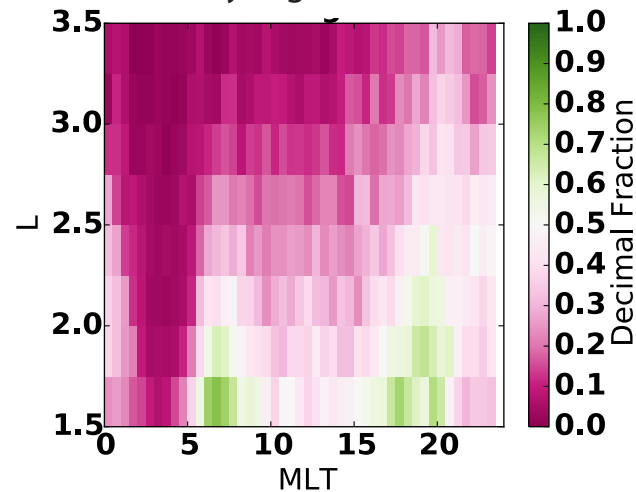
Low Wave

High Particle

High Wave and Particle

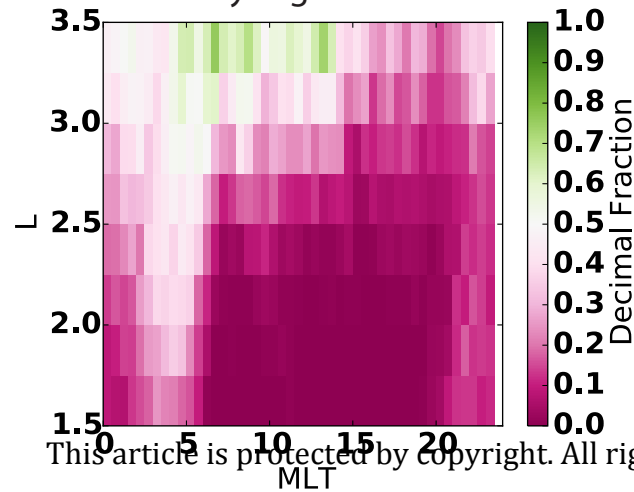


Only High Particle

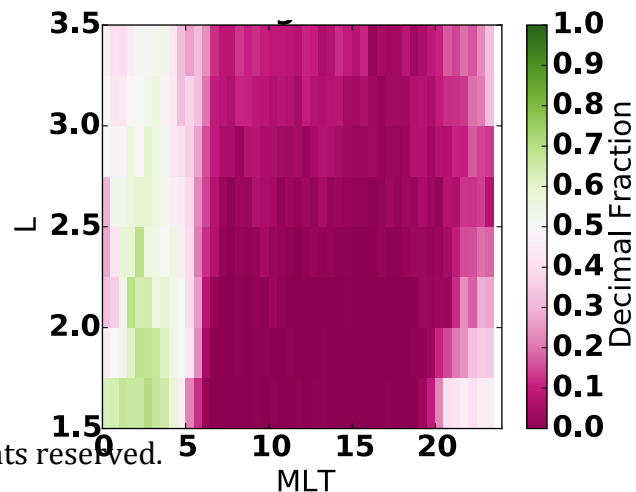


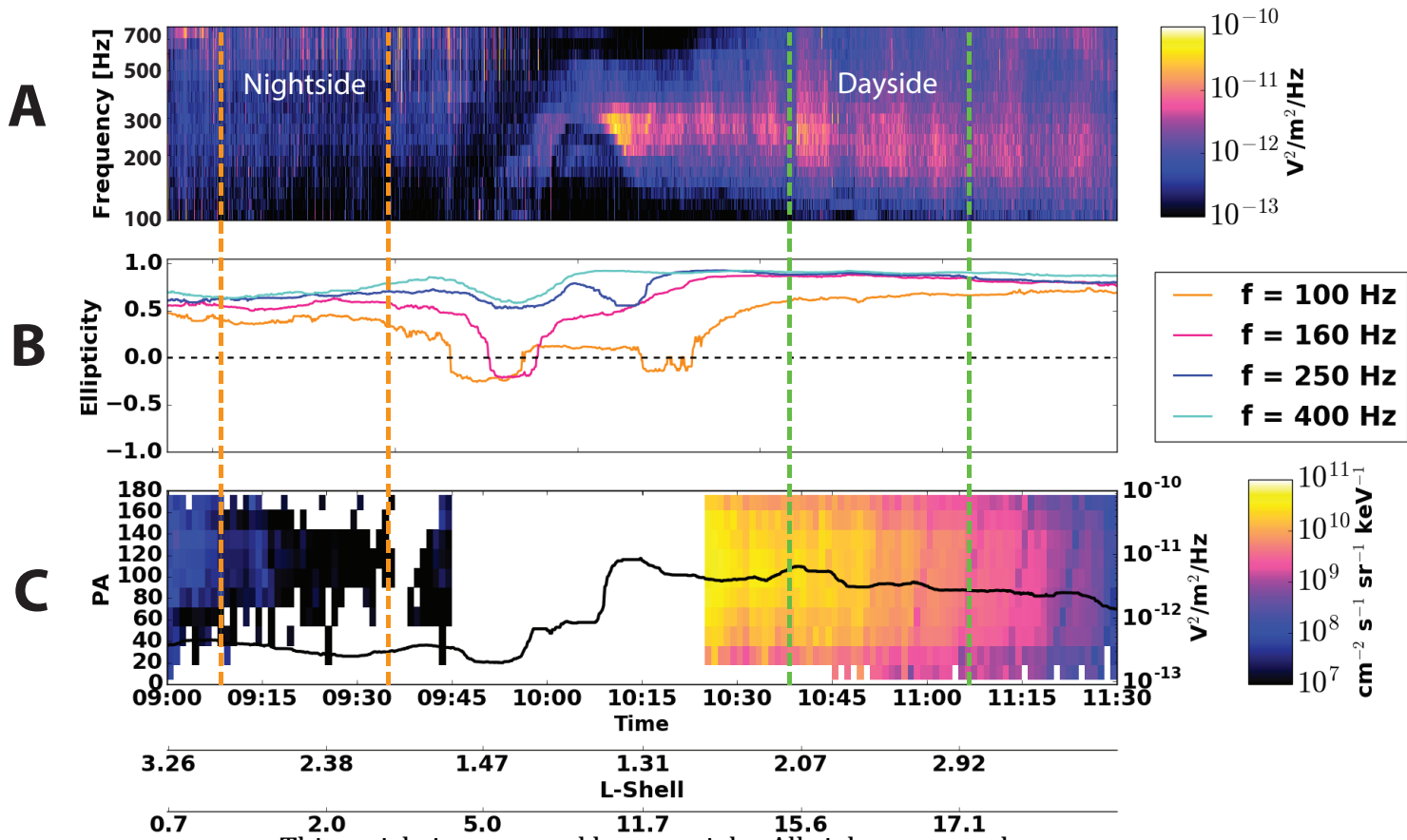
Low Particle

Only High Wave



Low Wave and Particle





Polarization between $2 < L < 3$

